

Direct Wigner tomography of a superconducting anharmonic oscillator

Yoni Shalibo¹, Roy Resh¹, Ofer Fogel¹, David Shwa¹, Radoslaw Bialczak², John M. Martinis² and Nadav Katz¹

¹*Racah Institute of Physics, The Hebrew University of Jerusalem, Jerusalem 91904, Israel and*

²*Department of Physics, University of California, Santa Barbara, California 93106, USA*

The analysis of wave-packet dynamics may be greatly simplified when viewed in phase-space. While harmonic oscillators are often used as a convenient platform to study wave-packets, arbitrary state preparation in these systems is more challenging. Here, we demonstrate a direct measurement of the Wigner distribution of complex photon states in an anharmonic oscillator - a superconducting phase circuit, biased in the small anharmonicity regime. We test our method on both non-classical states composed of two energy eigenstates and on the dynamics of a phase-locked wavepacket. This method requires a simple calibration, and is easily applicable in our system out to the fifth level.

The state of open quantum systems is frequently represented by a density matrix [1, 2]. This description is useful for a wide variety of systems, in which the probabilities and coherences in some chosen basis are of interest. However, in systems with continuous degrees of freedom, e.g. the relative position and momentum of atoms in a molecule, wavepackets are often formed and therefore phase space distributions are better suited to characterize the state and its dynamics [3]. In particular, the Wigner distribution offers direct information about expectation values and purity, and provides a convenient framework to test the quantum-classical correspondence [4, 5]. In addition, since the Wigner distribution holds complete information about the state, it can be directly transformed into a density matrix and therefore its measurement is useful for quantum state tomography [6] as well. Numerous experiments measured the Wigner distribution of harmonic systems using an auxiliary qubit [7, 8], or via heterodyne detection [9]. While anharmonic systems exhibit a wider variety of phenomena, a full quantum state reconstruction has so far been limited to atomic and molecular systems [10–13].

In this letter, we report on a direct measurement of the Wigner distribution in the Josephson phase-circuit, a superconducting anharmonic oscillator. Our method utilizes simple tomography pulses, and as opposed to standard state tomography, does not require individual calibration of the pulses.

Measuring the Wigner distribution in an anharmonic system poses several challenges. First, the phase of each level ϕ_n in the rotating frame advances in an increasing rate with n , causing wavepackets to disperse in phase space during the tomography pulse. For example, in a cubic potential this rate is given by $\dot{\phi}_n \approx \beta n(n-1)/2$, where $\beta = 2\pi(f_{10} - f_{21})$ is the anharmonicity and $n = 0, 1, 2, \dots$. Second, in our system it is impossible to measure the probability distribution in the phase space quadratures directly, and therefore the prominent method for phase-space tomography is measurement of the parity after a coherent displacement [8]. In order to achieve an approximate displacement operation, one has to apply a pulse which is simultaneously resonant with all

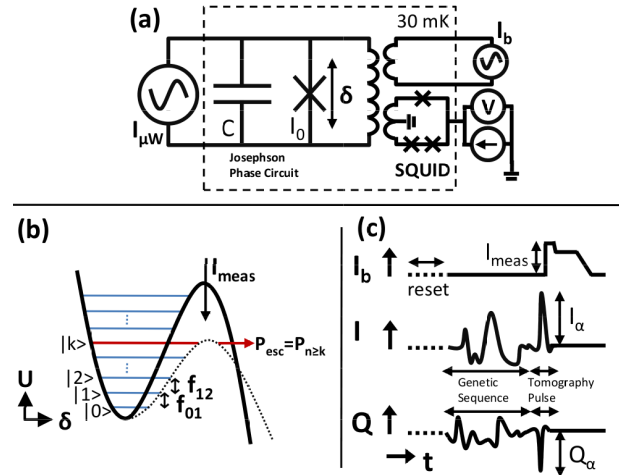


Figure 1: Experimental techniques. (a) The Josephson phase-circuit diagram. (b) Measurement of the occupation probabilities using short pulses in bias I_{meas} that cause selective tunneling of states $n < k$ which are detected later with an on-chip SQUID. (c) Time sequence of the Wigner tomography measurement of Fock-type superpositions.

the transitions within the measured subspace. We find that both restrictions can be practically met by both reducing the anharmonicity and applying sufficiently short tomography pulses.

Our system, the Josephson phase circuit (see Fig. 1a), is a superconducting LC oscillator with a weak anharmonicity, originating from a Josephson junction [14]. The potential energy of the system is one-dimensional and has the form of a double-well as a function of the phase difference δ across the junction. Using an external bias current I_b we tune the anharmonicity and measure the occupation probabilities of the energy levels inside the smaller potential well (see Fig. 1b). At large anharmonicity ($\beta/2\pi f_{01} \sim 0.02$), the lowest two levels are used for qubit operations via resonant microwave pulses $I_{\mu W}$ that yield high-fidelity gates of only a few nanoseconds in duration [15]. At small anharmonicity ($\beta/2\pi f_{01} \sim 0.002$), many more levels are accessible within a practical bandwidth and wave-packets can be easily generated [16]. In both

regimes the state is measured in the energy basis by applying a short pulse in I_b that causes selective tunneling of the probability in occupied levels $n > k$, where k depends on the height of the potential barrier, set by the pulse amplitude. Tunneling events are detected using an on-chip superconducting quantum interference device (SQUID), and for a set of measurement pulse amplitudes the occupation probabilities are reconstructed from the tunneling probabilities [16]. While standard state tomography (SST) can be used to measure the full density matrix of the lowest levels, in practice this method requires complicated calibration procedures for states with more than two levels, and is severely limited by decoherence. Our method requires only a single calibration measurement for all the tomography pulses, and can be scaled up to larger Hilbert spaces using optimized system parameters.

Ideally, the Wigner distribution is proportional to the expectation value of the parity operator after a coherent displacement [17]. Due to the finite anharmonicity in our system, we use short, gaussian-shaped resonant pulses as an approximate coherent displacement, while working at a weak anharmonicity. We control the phase and size of the complex displacement α by setting the phase and amplitude of the microwave pulse, using the relation $\alpha = -(1/2) \int \Omega(t) dt$ for a harmonic system, where $\Omega(t)$ is the time-dependent, gaussian-shaped Rabi amplitude. For our experimental parameters [18], the pulse is simultaneously resonant with many transitions between consecutive levels, ~ 6 of which are subject to an amplitude variation of less than 10% from the peak amplitude [19]. For a given anharmonicity β , a resonant pulse can be well approximated by a harmonic displacement in the limit $\beta T |\alpha|^2 / 4 \ll 1$, where $|\alpha|$ is the size of the applied displacement, m is the maximal occupied level after a displacement and T is the pulse duration [19]. This condition limits the maximal displacement to be well below the size of the distribution in phase space ($|\alpha_{max}| \ll 1$), for initial states occupying up to 5 of the lowest levels. However, we find in simulation that while the phases of the displaced state are very sensitive to the above condition, the probabilities are not, and therefore our approximation remains accurate for much larger displacements. We find that for our experiment parameters, up to 5 levels can be measured accurately. The expectation value of the parity operator is calculated from the measured occupation probabilities and is given by, $\alpha = (2/\pi) \sum_n (-1)^n P_n$ [17]. To test the effect of this pulse on our system, we initiate our system in the ground state and measure the occupation probabilities immediately after a short microwave pulse of total area α . Figure 2 shows the results of this measurement as a function of state number n and α (Fig. 2a), compared with the expected probabilities in a harmonic oscillator (Fig. 2b), $P(\alpha, n) = (1/n!) \exp(-|\alpha|^2) |\alpha|^{2n}$. As expected, the probability distribution in n is narrower compared to the

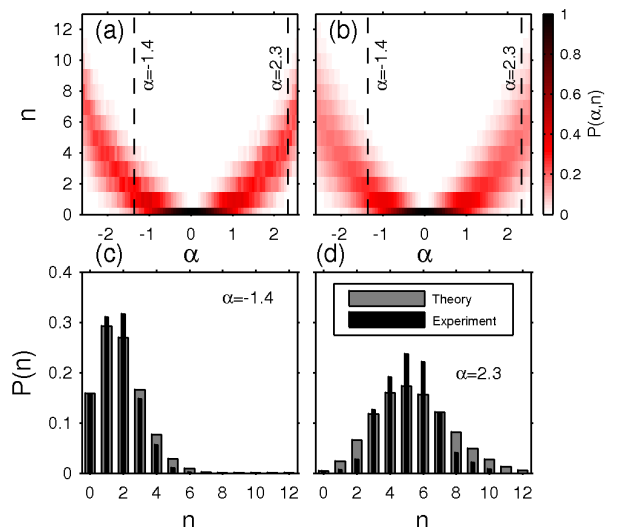


Figure 2: Tomographic pulse. Occupation probabilities for levels $n \leq 12$, as a function of $|\alpha|$ in the experiment (a) and theory (b). (c) and (d) show a histogram along the dashed lines shown in (a) and (b).

l	$P(0\rangle)$	$P(1\rangle)$	$P(2\rangle)$	$P(3\rangle)$	$P(4\rangle)$	$P(5\rangle)$	τ (ns)	χ (%)
1	0.52	0.47	0.01	0	0	0	15	99.8
2	0.69	0.05	0.24	0.02	0	0	30	93.4
3	0.58	0.03	0.11	0.27	0.01	0	25	90.5
4	0.70	0.01	0.03	0.07	0.17	0.02	40	88

Table I: Results of the optimization algorithm.

harmonic system for higher amplitudes due to our finite bandwidth. To compare the data and theory quantitatively, we plot a histogram of the distribution (Fig. 2c,d) for $\alpha = -1.3$ and $\alpha = 2.2$. At $\alpha = -1.3$ our data fits well with a harmonic displacement. At the largest displacement values ($\alpha = 2.2$) the deviation from harmonicity becomes more apparent as expected [19].

To benchmark our method, we apply it on a set of superpositions of eigenstates of the system, $|\psi_l\rangle = (|0\rangle + e^{i\phi} |l\rangle) / \sqrt{2}$ [20]. These states have a simple structure in phase space and cannot disperse since they contain one measurable phase that results in only a free rotation. As we operate our system in the small anharmonicity regime, preparing such states with high fidelity requires longer pulse sequences. Due to our short decay and coherence times ($T_1 = 120$ ns, $T_2 > 150$ ns) we apply optimized control sequences to reduce decoherence effects to a minimum (see Fig. 1c). We use a genetic optimization, where we define the population overlap $\chi = \overrightarrow{P_{ideal}} \cdot \overrightarrow{P_{meas}}$ and optimize it with a feed-back loop [19]. For a desired state $|\psi_l\rangle$, we set $\overrightarrow{P_{ideal}} = (0.5, 0, \dots, 0.5, 0, \dots)$ and use our measured occupation probabilities for $\overrightarrow{P_{meas}}$. The results of the optimization algorithm are summarized in Table 1.

As expected, χ decreases for a larger n , mostly due

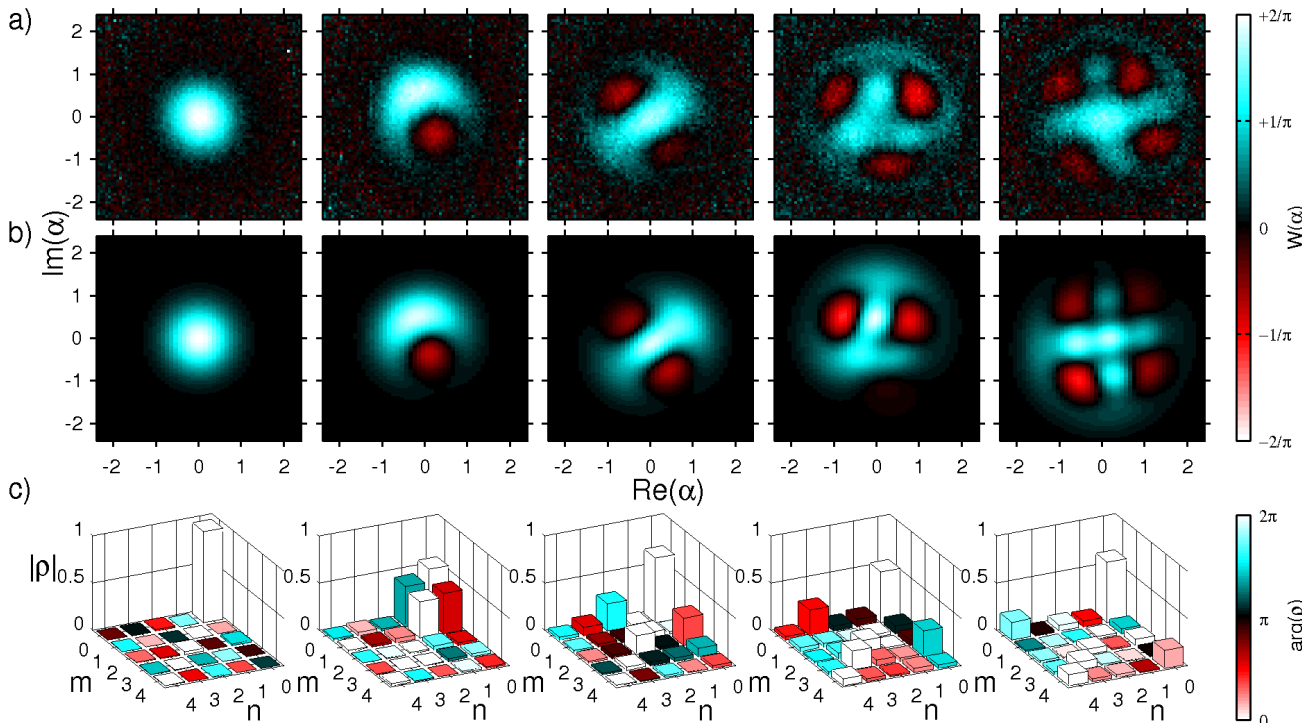


Figure 3: Superposition of Fock-type states. (a) Wigner tomography of genetically optimized superposition of fock-type states and (b) calculated Wigner distributions of these states, using level occupations from table 1 and phases of the extracted density matrices. (c) Extracted density matrices from the measurements shown in (a).

to our relatively short preparation pulse duration τ . To increase the value of χ for these states we increase τ , at the expense of the states' purity and optimization runtime. Our optimization algorithm does not take into account phases, however for sufficiently high values of χ , the Wigner image is dominated by only one phase, as can be seen in Fig. 3. In Fig 3a we plot the results of the tomography measurement on the ground state, and states $|\psi_l\rangle$ described in Table 1. These are compared with the expected images (Fig. 3b), calculated using the measured occupation probabilities, obtained independently by the optimization algorithm [21]. In Fig. 3c we plot the density matrices of the measured states, extracted using the harmonic oscillator wavefunctions. The diagonal elements in the extracted density matrices agree well with the measured occupation probabilities up to level $n = 4$. However, simulation shows that off-diagonal elements deviate increasingly for $n > 2$ [19]. We find that the origin of these errors is primarily the significant decay and decoherence that occur at highly excited levels during the tomography pulse, and secondarily the finite bandwidth of our tomography pulse. The errors in the measured Wigner distribution can be further reduced with currently available higher coherence samples [19].

In general, for any finite set of repetitions, the amount of information that is gained about the density matrix is smaller in a Wigner measurement relative to SST (assum-

ing equal number of repetitions and tomography pulses). This is due to the large overlap between the unitary operations associated with the Wigner tomography pulses, compared to the nearly orthogonal operations in a typical SST measurement. However, we find that the overhead in the number of repetitions in a Wigner measurement relative to SST with similar uncertainties is of order unity [19], thereby making the Wigner measurement a practical alternative for measuring the density matrix.

Non-dispersive wavepackets are particularly interesting to measure in phase space, due to phase-locking between the system and the drive that can take place within certain conditions [22]. In a system with negative anharmonicity ($f_{01} > f_{12}$), a negative frequency-chirped drive ($f_{drive} < 0$) can cause phase-locking at sufficiently large amplitudes, depending on the chirp rate and anharmonicity. To measure this effect, we initiate the system in the ground state and apply a negative frequency chirp, with a drive amplitude above the phase-locking threshold and a final frequency centered close to the transition frequency f_{23} . The chirp's temporal length and bandwidth $|f_{fin} - f_{in}|$ are chosen to be short (20 ns) and large (600 MHz) respectively, in order to have a broad excitation of states and for the excitation to be adiabatic [16]. Figure 4 shows the result at selected times along the chirp (Fig. 4a), and after the drive is turned off (Fig. 4b). The axes in the images are rotated at each

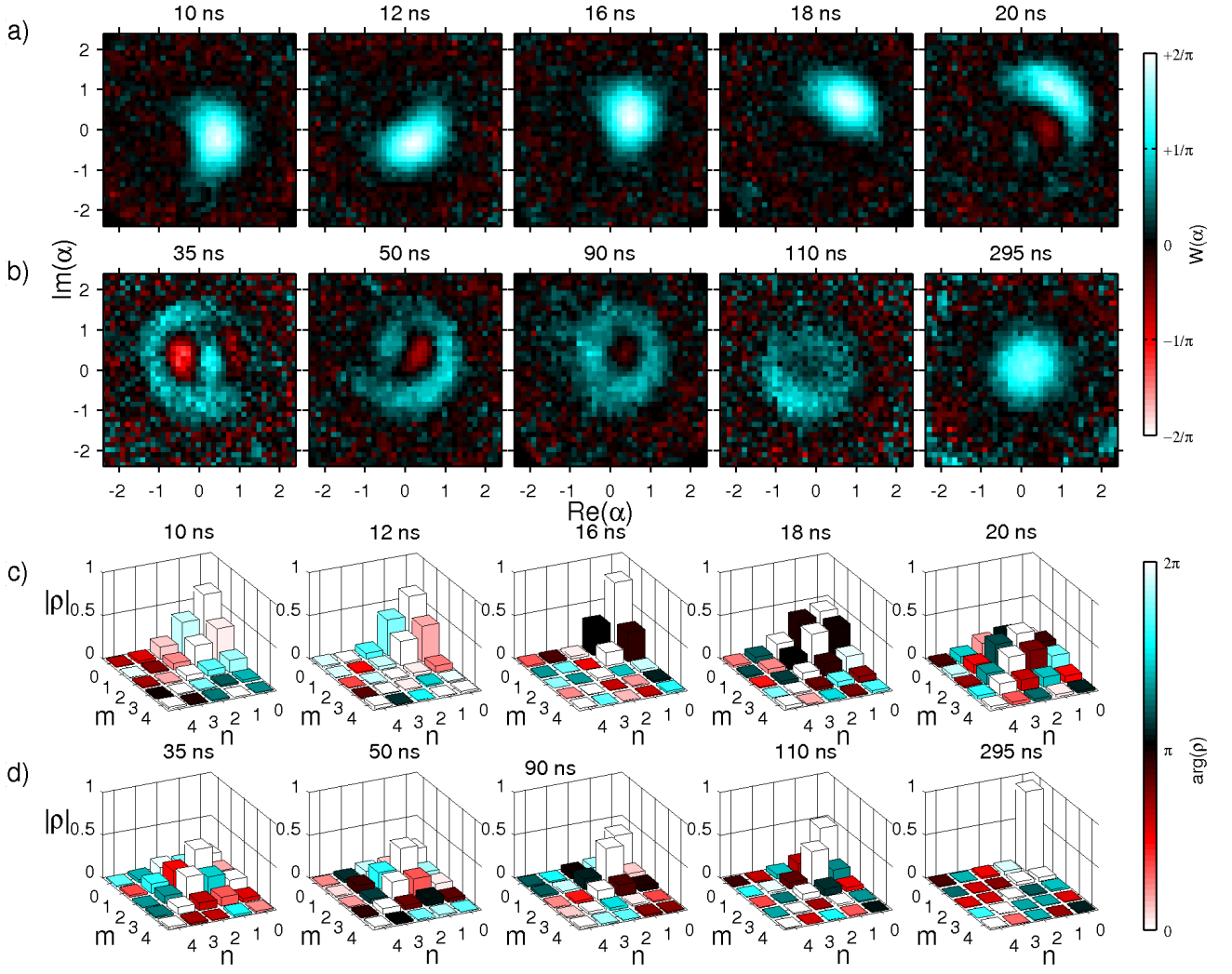


Figure 4: Dynamics of a phase-locked wave-packet. (a) Wigner tomography during a chirp ($T = 20$ ns, $\Omega/2\pi = 66$ MHz, $f_{in} - f_{01} = 320$ MHz, $f_{fin} - f_{01} = -50$ MHz), and (b) during drive-free evolution. (c) and (d) show the extracted density matrices for (a) and (b) respectively.

time frame to fit the rotating frame of the drive. During the chirp, we see a displacement of the ground state distribution that gradually acquires a constant phase as the drive crosses the linear resonance ($f = f_{01}$). This happens, as expected around $t = 16$ ns and the shape of the wavepacket becomes crescent-like. After the drive is turned off ($t = 21$ ns), phase-locking is lost and the wavepacket disperses due to the finite anharmonicity. At $t = 35$ ns, the state has completely dispersed, however it still contains significant coherences, as indicated by the negative values in the Wigner plot and the large off-diagonal elements in the extracted density matrix (Fig. 4d). The state then dephases into a ring shape which shrinks in radius towards the ground state. To track the decoherence dynamics in this experiment, we extract the state's purity evolution directly from the Wigner distribution: $\varphi = \pi \int d\vec{\alpha} |W(\vec{\alpha})|^2$ [3]. The result is shown

in Fig. 5 (red circles), and compared with a simulation (solid line). As expected, the purity remains high during the chirp, and then decays as a result of decoherence. The purity reaches a minimum and then ascends towards unity with an exponential rate, consistent with the measured decay time ($T_1 = 120$ ns) and in accordance with simulation.

In conclusion, we demonstrate a method of measuring the state of a multi-level system with a small anharmonicity in phase space. Using this method we are able to accurately extract the density matrix of up to 5 levels, limited by systematic errors caused by decoherence and finite bandwidth. This represents a significant improvement on standard state tomography which is difficult to implement in this subspace. The tunability of the phase circuit offers an approach of improving the accuracy of such a measurement at *larger* anharmonicity, by quickly

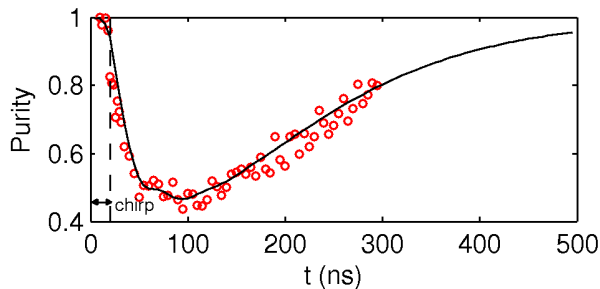


Figure 5: State purity. Extracted state purity φ from experiments (red circles) and simulation (solid line) during chirp and decay. The simulation includes the effect of the decay and dephasing and agrees with the measured decay time of $T_1 = 120$ ns.

changing the bias I_b after state preparation to the small anharmonicity regime where the tomography pulse is approximately a harmonic displacement. Finally, we point out that the overhead in the number of measurements required to extract the density matrix in a Wigner measurement is relatively small, and in addition one gains global information about the state faster than in standard state tomography.

This work was supported by ISF grant 1248/10 and BSF grant 2008438.

[1] M. Steffen *et al.*, *Science*, **313**, 1423 (2006).
 [2] L. DiCarlo *et al.*, *Nature*, **467**, 574 (2010).
 [3] W. P. Schleich, *Quantum Optics in Phase Space*, 1st ed.

(Wiley-VCH, 2001).
 [4] W. H. Zurek, *Rev. Mod. Phys.*, **75**, 715 (2003).
 [5] I. Katz, R. Lifshitz, W. Retzker and R. Straub, *New J. Phys.*, **10**, 125023 (2008).
 [6] M. A. Nielsen and I. L. Chuang, *Quantum Computation and Quantum Information* (Cambridge University Press, 2004).
 [7] P. Bertet *et al.*, *Phys. Rev. Lett.*, **89**, 200402 (2002).
 [8] M. Hofheinz *et al.*, *Nature*, **459**, 546 (2009).
 [9] C. Eichler *et al.*, *Phys. Rev. Lett.*, **106**, 220503 (2011).
 [10] T. J. Dunn, I. A. Walmsley, and S. Mukamel, *Phys. Rev. Lett.*, **74**, 884 (1995).
 [11] T. C. Weinacht, J. Ahn, and P. H. Bucksbaum, *Phys. Rev. Lett.*, **80** 5508 (1998).
 [12] E. Skovsen, H. Stapelfeldt, S. Juhl, and Klaus Molmer, *Phys. Rev. Lett.*, **91** 090406 (2003).
 [13] H. Hasegawa and Y. Ohshima, *Phys. Rev. Lett.*, **101** 053002 (2008).
 [14] J. Clarke and F. K. Wilhelm, *Nature*, **453**, 1031 (2008).
 [15] E. Lucero *et al.*, *Phys. Rev. A*, **82**, 042339 (2010).
 [16] Y. Shalibo *et al.*, *Phys. Rev. Lett.*, **108**, 037701 (2012).
 [17] A. Royer, *Phys. Rev. A*, **15** 449 (1977).
 [18] We use a 1.6 ns FWHM pulse and an anharmonicity $\beta/2\pi = 20$ MHz.
 [19] See supplementary material for more details on the genetic algorithm and a numerical analysis of errors.
 [20] ϕ is an unknown phase that can be determined via Wigner tomography. Since our optimization algorithm is only sensitive to state populations and not to phases, we cannot know it in advance.
 [21] Due to the non-negligible occupation probabilities we get at larger l states, we add phases to the Wigner distribution to account for additional features in the image
 [22] J. Fajans and L. Friedland, *Am. J. Phys.*, **69**, 1096 (2001).

Direct Wigner tomography of a superconducting anharmonic oscillator

Yoni Shalibo, Roy Resh, Ofer Fogel, David Shwa, Radoslaw Bialczak, John M. Martinis and Nadav Katz

Supplementary Information

Materials and methods. The Josephson phase circuit [1] used in the experiment has the following design parameters: critical current $I_0 \approx 1.5 \mu\text{A}$, capacitance $C \approx 1.3 \text{ pF}$ and inductance $L \approx 940 \text{ pH}$. The qubit has a tunable frequency f_{01} in the 6-9 GHz range. During the experiment the device is thermally anchored to the mixing chamber of a dilution refrigerator at 30 mK, where thermal excitations of the qubit are negligible.

We use a custom built arbitrary waveform generator (AWG) having a fast (1 ns time resolution), 14-bit digital-to-analog converter to shape the microwave pulses which control the quantum state of the circuit. We control the phase and amplitude of the drive by modulating a high-frequency oscillator of frequency f_{LO} with the AWG, using an IQ-mixer. The modulation signals are fed into the I and Q ports of the IQ-mixer to give an amplitude $\sqrt{I(t)^2 + Q(t)^2}$ and a relative phase $\phi(t) = \arctan(Q(t)/I(t))$ at its output.

Harmonic response. As indicated in the manuscript, the bandwidth of the tomography pulse must be large relative to the anharmonicity, for a nearly harmonic response. This is easily understood by looking at the position of the transitions in the spectral domain, relative to the local oscillator frequency (see Fig. S1). As seen in the figure, the effective drive amplitude of the lowest 6 transitions is the same, to within a 10% variation. This is consistent with our data and simulations (see Sec. II), showing small systematic errors within the corresponding subspace. In principle, more transitions can fit within this region by positioning the local oscillator lower in frequency.

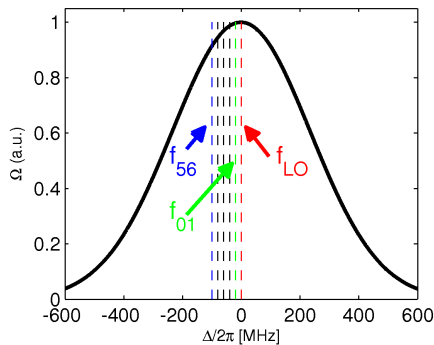


Figure S1: Tomography pulse envelope in the frequency domain. Dashed lines are the lowest five transitions $f_{n,n+1}$ and the local oscillator frequency position in the experiment. The pulse envelope (solid line) is the normalized fourier transform of a 1.6 ns FWHM gaussian function.

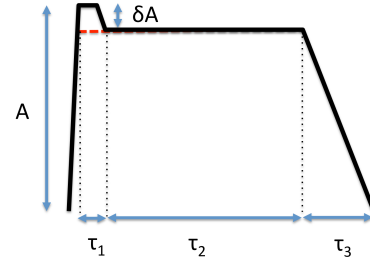


Figure S2: Measurement pulse used in the experiment. All the pulse parameters except for the total amplitude A are fixed.

Populations measurement. The measured escape probabilities due to a set of experiments with different measurement pulses are converted into level occupation probabilities using the measured escape curves of the lowest levels in the well [2]. In this experiment, we used a novel measurement pulse shape, to reduce distortions of the escape curves of higher levels. This measurement pulse is shown in Fig. S2. Typically, one must use a pulse with a slowly decaying end, in order to reduce the effect of population re-trapping in the original well after the pulse ends. The effect of re-trapping becomes more prominent as the anharmonicity is reduced due to the corresponding deepening of the potential well, and therefore requires increasing both τ_2 and τ_3 to eliminate re-trapping. At the working bias point used in our experiment, we use $\tau_2 = 25 \text{ ns}$ and $\tau_3 = 15 \text{ ns}$. These parameters are non-negligible relative to the decay time and cause artificial increase of the extracted population at lower levels, which in turn distorts the Wigner image. To avoid this effect we add a small step in amplitude at the beginning of the pulse ($\tau_1 = 1 \text{ ns}$) to preselect the population we want to escape, and then reduce the amplitude by an amount δA . Even the small difference δA is sufficient to protect undesired population at lower levels from tunneling out during the long waiting time in which the escaped population decays in the external well.

Density matrix fit. In the Wigner tomography experiments we extract the density matrix from the populations of the displaced states [3]. We use 200 homogeneously distributed random displacements within a $|\alpha| < 2$ circle to fit the density matrix, while restricting the density matrix to a 6×6 subspace. It should be noted that both the measured Wigner distribution and the extracted density matrix represent the state after a rotation that occurs during the tomography pulse. To get more accurate phases, one can apply an inverse propagator on the density matrix $U = \exp(-iH_0\Delta t/\hbar)$, where

H_0 is the drive-free Hamiltonian and Δt is the effective pulse length for the rotation.

STATE PREPARATION BY GENETIC OPTIMIZATION

Finite anharmonicity makes it possible to prepare states, composed of arbitrary superpositions of eigenstates within our system. However, Fourier broadening of the drive, together with power broadening of the transition energies causes nontrivial excitation at relatively small anharmonicities. Adding the short decay and coherence time, it becomes challenging to prepare a desired, yet pure state. We solve this difficulty, by optimizing the state produced with a feedback from the experiment. Our target state in the optimization algorithm is a superposition of eigenstates of our system: $|\psi_l\rangle = (|0\rangle + e^{i\phi}|l\rangle)/\sqrt{2}$. Using the measured probabilities we are able to optimize such a superposition up to an unknown phase ϕ that causes only a free rotation of the measured Wigner function.

Our optimization algorithm is based on guided evolution. It is constructed in the following steps:

(a) We define a set of N_G pulse sequences (genomes). Each genome is a sequence of N_t complex numbers that represent the amplitude and phase of the drive's pulse envelope at each time step, with 1 ns time resolution. In addition, each genome is associated with a population overlap, defined as: $\chi = \overrightarrow{P_{ideal}} \cdot \overrightarrow{P_{meas}}$, where $\overrightarrow{P_{ideal}}$ and $\overrightarrow{P_{meas}}$ are the desired and measured population vectors. The genomes are initialized with random complex numbers, each having a maximal amplitude Ω_{max} , and $\chi = 0$.

(b) At each iteration of the algorithm (generation), we assume that the current set of genomes is sorted in order of decreasing χ . The upper N_a genomes are kept, and the next N_a genomes are replaced by a combination of the upper $N_a + 1$ genomes: $\overrightarrow{G_{N_a+k}} = \overrightarrow{P}(G_k, G_{k+1}) + \overrightarrow{c}$, where the function $\overrightarrow{P}(x, y)$ randomly selects an amplitude between the sets x and y at each time step and \overrightarrow{c} is a set of random complex numbers with a small amplitude ϵ_{max} (noise). The bottom $N_G - 2N_a$ genomes are replaced by random complex numbers with an amplitude Ω_{max} .

(c) The bottom $N_G - N_a$ genomes of the next generation are then applied and the resulting probabilities $\overrightarrow{P_{meas}^k}$ for each genome are measured. After calculating χ of each, we sort our new set G in order of decreasing χ , and mark genome sequences that have (potentially) higher χ than the current optimal χ . For each genome having a potentially higher χ we repeat the measurement N_{rep} times, recalculate χ and reposition them in the set G . Step (b) is run again.

Fidelity measure. Our population overlap χ measures the distance between two states. There are many

possibilities of defining the fidelity, and in general each gives a different bias for the algorithm towards finding a specific family of states. In our definition for example, χ is highly sensitive to the overall population that exists outside the subspace that is populated in the target state. However it is much less sensitive to the distribution among levels that are populated in the target state. Our definition is particularly useful for optimizing our target states $|\psi_l\rangle$ for a Wigner measurement, because we wish to eliminate the population of states other than $|0\rangle$ and $|l\rangle$.

There are two important factors that limit the performance of any optimization algorithm in experimental systems: shot noise, and drifts in the physical parameters of the system.

Shot noise. Any finite number of repetitions results in some uncertainty in the measured probabilities. To determine n occupation probabilities in the final state we measure the tunneling probabilities after n measurement pulses having different amplitudes. In a typical optimization algorithm, we repeat the measurement of a single tunneling probability 900 times. Statistical analysis gives a typical uncertainty (standard deviation) of $\sim 2\%$ in χ for sufficiently high values of χ ($\chi \gtrsim 80\%$) and therefore one cannot distinguish between two genomes with a χ difference which is smaller than $\sim 3\%$. We therefore expect the algorithm to run significantly more slowly at χ 's approaching unity, due to false increase of χ . To increase the efficiency of the algorithm without increasing the number of repetitions of each measurement, we repeat the measurement only for genomes with potentially increased χ , as described in step (c).

Drifts. The response of the system to the application of a given genome can change in time due to drifts in its physical parameters. We correct for drifts in the energies by performing a spectroscopic measurement of the qubit transition frequency every 10 minutes and adjusting the flux bias to restore the qubit frequency to its original value. In addition, we correct for drifts in the offset voltages applied to the IQ mixer that eliminate leakage of the microwave drive while it is turned off.

SYSTEMATIC ERRORS

To quantify the errors in the measured Wigner function and density matrix caused by finite anharmonicity and decoherence, we perform numerical simulations. In our simulations, we propagate an anharmonic system, initialized with a pure state $\rho = |\psi\rangle\langle\psi|$, with resonant pulses. Each pulse is assumed to be resonant with the first transition and has a gaussian envelope with the same width as in the experiment. We use the rotating wave approximation for constructing the Hamiltonian, and neglect corrections to the drive coupling beyond the harmonic approximation, namely $\langle n | \delta | m \rangle = 0$ for $n \neq m \pm 1$ and

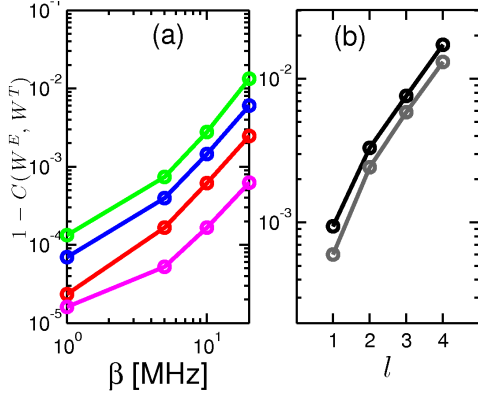


Figure S3: Systematic errors in the Wigner distribution, for initial states $|\psi_l\rangle = (|0\rangle + |l\rangle)/\sqrt{2}$, where $l = 1, 2, 3, 4$. The cross-correlation deviation as a function of the anharmonicity (a) and initial state. In (a), decoherence is not included, and the magenta, red, blue, green lines correspond to the initial state $l = 1, 2, 3, 4$ respectively. In (b) decoherence is included and the anharmonicity is fixed to $\beta = 20$ MHz. The black and grey lines correspond to decoherence parameters $T_1 = 150$ ns, $T_2 = 200$ ns and $T_1 = 600$ ns, $T_2 = 600$ ns respectively.

$\langle n | \delta | m \rangle = \sqrt{n}, \sqrt{n+1}$ for $m = n \pm 1$. This results in the following time dependent unitary propagator: $U(t) = \exp(i \frac{\delta t}{2} [(\Omega(t)a^\dagger + \Omega(t)^*a) + \beta a^\dagger a (a^\dagger a - 1)])$, where δt is the time step in the simulation, $\Omega(t)$ is the time dependent drive envelope amplitude and $\beta = 2\pi(f_{01} - f_{12})$ is the anharmonicity. Decoherence and energy relaxation are taken into account using quantum operations, assuming only two phenomenological parameters: the energy relaxation time of the qubit T_1 and its pure dephasing time T_2 .

We expect to have negligible systematic errors due to finite anharmonicity when the second term in the exponent of the propagator becomes negligible. By separating the terms in the exponent to first order, and assuming a constant drive amplitude Ω of total duration T , we can approximate the propagator to $U \approx D(\alpha) \exp(-i \frac{T\beta}{4} [(a a^\dagger - \alpha^* a), a^\dagger a (a^\dagger a - 1)])$ where $D(\alpha)$ is the displacement operator and $\alpha \equiv i\Omega T$. The second term can be considered negligible in the limit, $|\alpha| T \beta m^2 / 4 \ll 1$, where m is the maximal occupied state. For our experimental parameters ($\beta/2\pi = 20$ MHz, $T = 1.6$ ns), the second term can be neglected only for $|\alpha| \ll 1$, however, the error in the Wigner distribution, obtained from the state populations after the pulse are negligible even for $\alpha \approx 2$, as we show in our analysis.

We plot the errors in the Wigner distribution and the extracted density matrices, as a function of the anharmonicity β , initial state, and decoherence parameters. The density matrix is extracted, as in the experimental data, using only the populations of the lowest 6 levels.

To quantify the error in the Wigner distribution, we calculate the cross-correlation (at zero offsets) be-

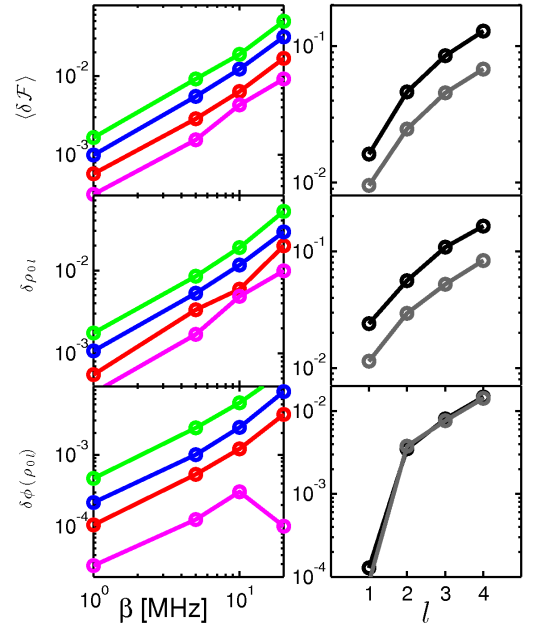


Figure S4: Systematic errors in the extracted density matrix, for initial states $|\psi_l\rangle = (|0\rangle + |l\rangle)/\sqrt{2}$, where $l = 1, 2, 3, 4$. The left column of plots shows the fidelity error, and errors in the off-diagonal matrix element ρ_{0l} as a function of anharmonicity, in the absence of decoherence. The magenta, red, blue and green lines correspond to the initial state $l = 1, 2, 3, 4$ respectively. The same error measures are plotted in the right column, as a function of initial state l , with decoherence included, at $\beta = 20$ MHz. The black and grey lines correspond to decoherence parameters $T_1 = 150$ ns, $T_2 = 200$ ns and $T_1 = 600$ ns, $T_2 = 600$ ns respectively.

tween the ideal Wigner distribution of the initial state, and the one obtained from the expectation value of the parity operator after a set of displacements. The cross correlation is defined as $C(f(x, y), g(x, y)) = \sum_{x', y'} \frac{(f(x', y') - \langle f \rangle)(g(x', y') - \langle g \rangle)}{\sqrt{\sum_{x'', y''} (f(x'', y'') - \langle f \rangle)^2 \sum_{x, y} (g(x'', y'') - \langle g \rangle)^2}}$, where $\langle f \rangle, \langle g \rangle$ are the average values of f, g . The results are plotted in Fig. S3. As seen in the figure, the error increases sharply with both anharmonicity and maximal populated level l .

To quantify the error in the extracted density matrices, we use the standard fidelity definition: $\langle \delta \mathcal{F} \rangle = 1 - \text{Tr} \sqrt{\sqrt{\rho^F} \rho^I \sqrt{\rho^F}}$, where ρ^I is the initial density matrix and ρ^F is the density matrix obtained from a fit to the populations of the displaced states. We choose the initial density matrix ρ^I to be $|\psi_l\rangle \langle \psi_l|$, where $|\psi_l\rangle = (|0\rangle + |l\rangle)/\sqrt{2}$. In addition, we calculate the error in the non-zero off-diagonal elements of the density matrix using the following definitions: $\delta \rho_{0l} = ||\rho_{0l}^F| - |\rho_{0l}^I||$ is the error in the amplitude of the matrix element, and $\delta \phi(\rho_{0l}) = |\phi(\rho_{0l}^F) - \phi(\rho_{0l}^I)|/2\pi$ is the normalized error in the phase of the matrix element.

As seen in the Fig. S4, all the error measures are negligible (smaller than ~ 0.05) when decoherence is

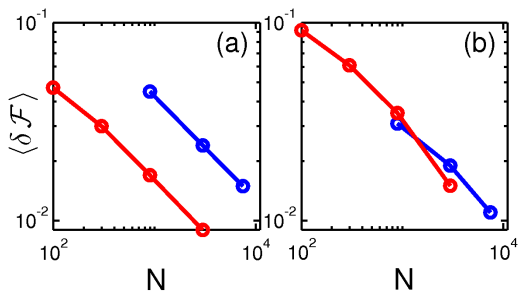


Figure S5: Error in the fidelity due to shot noise in standard state tomography and WT. $\langle \delta \mathcal{F} \rangle$ vs. N in WT (blue) and SST (red) of the initial states $|\psi\rangle = (|0\rangle + |4\rangle)/\sqrt{2}$ (a) and $|\psi\rangle = (1/\sqrt{5}) \sum_{k=0}^4 |k\rangle$ (b). Both follow the $1/\sqrt{N}$ trend.

neglected. However, when included, both the fidelity and the amplitude of the off-diagonal elements have non-negligible errors. For currently available samples having $T_1 > 600$ ns, and correspondingly longer T_2 , the errors due to decoherence can be substantially reduced; In this case, the errors become smaller than 0.1 in all the measures. As expected, the phase error is quite insensitive to decoherence.

SHOT NOISE IN WIGNER TOMOGRAPHY VS. STANDARD STATE TOMOGRAPHY

As pointed out in the manuscript, phase space is a convenient basis to experimentally acquire global information about the state (e.g. phase distribution, average energy etc.) *fast*, on the expense of accurate knowledge of the state in the eigenstate basis. Therefore, when extracting the density matrix in the latter basis from a Wigner measurement, one requires an excess number of measurements compared to standard state tomography (SST) to achieve similar uncertainties. It turns out that this is only true for a certain class of states. For states that are dispersed in phase space, such as states composed of a coherent superposition of a small number of eigenstates, SST requires significantly less tomography pulses than Wigner tomography (WT) to achieve a comparable error in the density matrix but the *same* number of pulses for states that are localized in phase space. The overhead in the number of measurements is an important parameter from an experimental standpoint, and therefore we perform numerical simulations to calculate it. In the following we describe our simulation methods for both cases.

WT. We start with a pure initial state $|\psi\rangle$. We use the same method described in Sec. II to calculate the density matrix after a coherent displacement. We keep the diagonal elements of the final density matrix, for a set of N_W random displacements α that are uniformly dis-

tributed in the complex plane. For each experiment (a particular displacement) we calculate an ensemble of M possible outcomes for the measurements of the diagonal elements, assuming r repetitions in the experiment, and a binomial distribution for the escape probabilities, from which the diagonal elements $P(n)$ are calculated. For each outcome, we extract the density matrix and calculate its fidelity $\mathcal{F} = \text{Tr} \sqrt{\sqrt{\rho^{tom}} \rho^{ideal} \sqrt{\rho^{tom}}}$. We then calculate the average fidelity $\langle \mathcal{F} \rangle$ of the ensemble to find the experimental error $\langle \delta \mathcal{F} \rangle = 1 - \langle \mathcal{F} \rangle$ due to shot noise.

SST. We start with a pure initial state $|\psi\rangle$. We construct a set of $N_{SST} = d^2$ orthogonal, unitary operations U_j to span a d -level subspace. The set of operations is chosen to be the generators of $SU(n)$ for convenience. From the diagonal elements of the rotated density matrices, we are able to extract the expectation values of each generator $\langle U_j \rangle = \text{Tr}(\rho U_j)$, and therefore reconstruct the original density matrix: $\rho = \sum_j \langle U_j \rangle U_j$ [4]. As before,

for each diagonal we calculate an ensemble of M possible measurement outcomes due to shot noise. From each of the measurements in the ensemble, we extract the expectation values of the operators U_j and calculate the corresponding density matrix. The average fidelity error of the ensemble of density matrices is then evaluated.

Figure S5 shows the results of both simulations. We plot $\langle \delta \mathcal{F} \rangle$ as a function of $N = R$, where R is the number of repetitions of the experiment per tomography pulse. In the WT simulation we define N relative to the SST case: $N = R \left(\frac{N_W}{N_{SST}} \right)$, where N_W is the number of tomography pulses in the Wigner simulation, and N_{SST} is the number of tomography pulses in SST. While N_{SST} is fixed, we vary N in the WT simulation by using many displacement pulses while fixing R , and in the SST simulation we vary N by changing the statistics R . In all Wigner simulations we fix R to be 900 (as in our experiment) and in the SST simulations we vary R from 100 to 3000.

We see that for an initial state, composed of a coherent superposition of only 2 states (Fig. S5a), SST outperforms WT by a factor of 8, in terms of the fidelity \mathcal{F} . In contrast, for states composed of a coherent superposition of 5 eigenstates, the amount of information that is extracted per pulse in SST and WT is similar. This is because our chosen state is partially localized in phase space, and therefore requires less displacement pulses to extract its properties.

-
- [1] J. M. Martinis, S. Nam, J. Aumentado, C. Urbina, Phys. Rev. Lett., **89**, 117901 (2002).
 - [2] Y. Shalibo et al. Phys. Rev. Lett., **108**, 037701 (2012).
 - [3] M. Hofheinz *et al.*, Nature, **459**, 546 (2009).
 - [4] R. T. Thew, K. Nemoto, A. G. White, W. J. Munro, Phys. Rev. A, **66**, 012303 (2002).